MID-AMERICA TRANSPORTATION CENTER

Report # MATC-MS&T: 139-3

Final Report

WBS: 25-1121-0005-139-3

Understanding of Bridge Vulnerability to Climate Change Enables Pro-active Adaptation Measures

Grace Yan, PhD
Associate Professor
Department of Civil, Architectural and Environmental Engineering
Missouri University of Science and Technology

Hunter Boswell
PhD Student
Department of Mechanical and Aerospace Engineering
Missouri University of Science and Technology

2023

A Cooperative Research Project sponsored by U.S. Department of Transportation- Office of the Assistant Secretary for Research and Technology

MATC

Understanding of Bridge Vulnerability to Climate Change Enables Pro-active Adaptation Measures

Grace Yan, PhD
Associate Professor
Department of Civil, Architectural and Environmental Engineering
Missouri University of Science and Technology

Hunter Boswell
PhD Student
Department of Mechanical and Aerospace Engineering
Missouri University of Science and Technology

A Report on Research Sponsored by

Mid-America Transportation Center

University of Nebraska–Lincoln

January 2023

Technical Report Documentation Page

1. Report No. 25-1121-0005-139-3	2. Government Accession No.	3. Recipient's Catalog No.
4. Title and Subtitle Understanding of Bridge Vulnerability to Climate Change Enables Pro-active Adaptation Measures		5. Report Date Jan. 15, 2023 6. Performing Organization Code
7. Author(s) Grace Yan and Hunter Boswell		8. Performing Organization Report No. 25-1121-0005-139-3
9. Performing Organization Name and Address Missouri University of Science and Technology 1401 N. Pine St. Rolla, MO 65401		10. Work Unit No. (TRAIS) 11. Contract or Grant No. 69A3551747107
12. Sponsoring Agency Name and Address Office of the Assistant Secretary for Research and Technology 1200 New Jersey Ave., SE Washington, D.C. 20590		13. Type of Report and Period Covered Final Report January 2021-December 2021 14. Sponsoring Agency Code MATC TRB RiP No. 91994-87
15. Supplementary Notes		

16. Abstract

In the past few decades, climate change has been leading to more severe hurricanes. Hurricanes have been identified as the starting point of weather-related disasters in coastal regions due to their coincident generation of extreme winds, high storm surge, strong waves, and heavy rainfall. Bridges in coastal regions are exposed to these multi-hazards. To mitigate these threats, to increase the resilience of bridges, and to take pro-active adaptation measures, the overarching goal of this research project is to apply multi-phase direct numerical simulation to understand the wind-surge-wave interaction, which will be used to better quantify the combined loading on bridges from multiple hazards. The obtained results can be used to inform the improvement of the AASHTO Bridge Design Specifications to accommodate the future climate change, enhancing the resilience of bridges.

17. ORCID No. of each Researcher	18. Distribution Statement		
19. Security Classif. (of this report) Unclassified	20. Security Classif. (of this page) Unclassified	21. No. of Pages 40	22. Price

Table of Contents

List of Figures

List of Tables

Disclaimer

The contents of this report reflect the views of the authors, who are responsible for the facts and the accuracy of the information presented herein. This document is disseminated in the interest of information exchange. The report is funded, partially or entirely, by a grant from the U.S. Department of Transportation's University Transportation Centers Program. However, the U.S. Government assumes no liability for the contents or use thereof.

Abstract

In the past few decades, climate change has been leading to more severe extreme weather (e.g., hurricanes and heat waves), quicker sea-level rise, and more frequent flooding in coastal regions. In particular, hurricanes have been identified as the starting point of weather-related disasters in coastal regions due to their coincident generation of extreme winds, high storm surge, strong waves, and heavy rainfall. Bridges in coastal regions are exposed to these multi-hazards. To mitigate these threats, to increase the resilience of bridges, and to take pro-active adaptation measures, the overarching goal of this research project is to apply multi-phase direct numerical simulation to understand the wind-surge-wave interaction, which will be used to better quantify the combined loading on bridges from multiple hazards. The obtained results will inform decision-makers when they develop near-term measures and long-term plans for mitigation and adaptation to climate change. The obtained results can be used to inform the improvement of the AASHTO Bridge Design Specifications to accommodate future climate change, enhancing the resilience of bridges.

Chapter 1 Research Motivation and Significance

During a storm surge, as water waves approach a beach or shore, they steepen and break, dissipating the energy that they have gained well away from the shore. Given that the impact of coastal storms on bridges has become more severe in recent years owing to climate change and increased urban development, there has been an increasingly urgent need to understand the loadings that such breaking waves exert on coastal and offshore infrastructure, such as the bridges used in this project, particularly in the presence of other storm-related phenomena, such as strong winds and storm surges [1]. There is also a fundamental interest in breaking waves: deep water breakers modulate mass, momentum, and energy transfer between the ocean and the atmosphere [2], while in the nearshore environment they play a strong role in dissipating wave energy [3–5], the development of currents [3,5–7], runup and setup of the shoreline water level [3,6,8], and transport of sediment and biological material via turbulent dissipation [7,9]. A physical understanding of these phenomena is crucial for the development of robust parametrizations used in modeling wave systems and, ultimately, the dynamics of the ocean and atmospheric processes [1].

Although the shallow-water wave breaking process has been studied for many years, its complete understanding remains elusive. To study the fundamental dynamics of shoaling breakers, simplified bathymetries such as uniform slopes or step transitions in depth are often utilized. The problem of wave propagation into an inundated area (such as by storm surge) may be modeled by a change in depth with a linear slope transition (see Fig. 1.2 below); the dynamics of individual breakers may then be clearly examined by the propagation of a solitary wave over such a bathymetry. Such a problem has not to our knowledge been extensively investigated, aside from an analytical examination conducted by Bautista et al. [10]. In fact, most investigations have

considered a uniform beach without an inshore inundated region [11–20], an abrupt change in depth, such as over a bathymetric shelf [21–27], or a submerged breakwater [28,29].

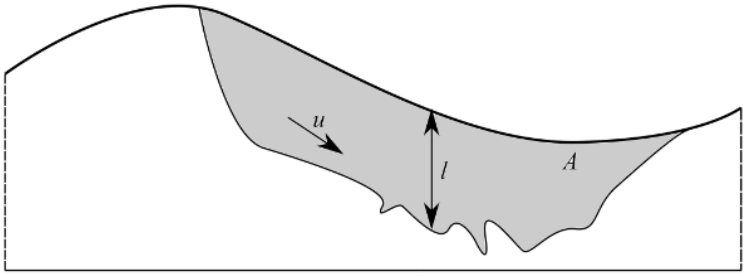

Figure 1.1 Turbulent zone formed by the wave after breaking, showing the relevant integral velocity scale u, length scale l, and cross-sectional area A. The relationship between these scales and the wave parameters is unchanged between deep and shallow water, except for l. Adopted from Drazen et al. [46] [Fig. 1(c)].

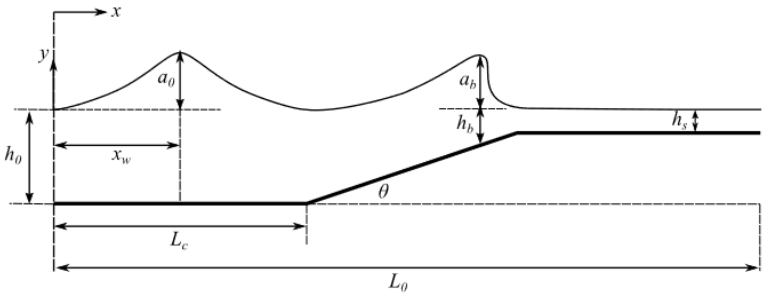

Figure 1.2 Schematic diagram of wave breaking process. Conditions are shown at initialization and at point of breaking. When the wave breaks, the leading interface of the wave becomes vertical, and the wave amplitude ab is measured at this instant.

Configurations such as these are useful for gaining an understanding of the small-scale physics of wave propagation, steepening, and breaking; this understanding can then be used to improve large-scale modeling efforts. Aside from experimental methods, a variety of wave-resolving numerical models and tools have been used to understand these simple systems. Large-

eddy simulation is used for understanding phenomena at and above the individual wave scale but relies on assumptions for the small-scale processes involving turbulence and void-fraction effects. Fully nonlinear potential flow models [19,30] are especially powerful for understanding the evolution of prebreaking waves but cannot capture the breaking process itself or the associated dissipative processes. However, with increasing sophistication of numerical methods and availability of computational resources, it has become possible in recent years to use direct numerical simulation (DNS) in simulating the wave breaking process [20,31–35]. While the main drawback of DNS is that it is too computationally expensive to simulate intermediate- or large-scale wave systems, DNS of wave breaking nevertheless provides a powerful investigative tool for understanding the small-scale physics of breakers directly. Somewhat surprisingly, this has proven to be the case for two-dimensional (2D) simulations, despite the essentially three-dimensional (3D) character of turbulence: many investigations by different authors across a variety of different experimental and numerical setups have shown that 2D numerical breakers experience dissipation rates similar to 3D numerical and experimental breakers [33–36], although naturally slightly smaller; this remains the topic of ongoing investigation [35]. On the basis of these observations, and following [20], we will assume here that 2D simulations are a reasonable proxy for the energetic dissipation of the full 3D simulations, subject to confirmation in a future study.

The purpose of the present study is to perform DNS of a breaking solitary wave on a simple bathymetry in the presence of a storm surge. The resulting data will then be used to set up physics-informed parametrizations for wave energy dissipation in storm surge conditions, for future applications to larger-scale models that operate under more realistic topographies and bathymetries, such as Simulating WAves Nearshore (SWAN). We will present a 2D DNS of solitary breakers approaching an inundated beach with the configuration shown in Figure 1.2. Solitary waves have

long been used as models for studying breaking processes (e.g., [11,12,37]). In this project, we will include an inundated inshore beach region, which allows the broken wave to propagate over a region of uniform depth. In the analysis, the generality of parametrizations and relevance of scaling arguments usually applied to deep-water systems will also be discussed. The remainder of this report is organized as follows. In Chapter 2, we will review existing physics-based parametrizations for energy dissipation in breaking waves, which will be tested against new data in Chapter 4. In Chapter 3, the problem itself will be formulated and the methodology will be presented. In Chapter 4, we will present the data, test the various parametrizations against it, and discuss insights that may lead to a general water-depth-independent parametrization. Finally, in Chapter 5, conclusions will be drawn, and future work will be suggested.

Chapter 2 Review on Model Parametrizations for Wave Breaking

The project will use DNS to generate high-resolution data that can inform the development of strictly physics-informed parametrizations for wave breaking in shallow water. Therefore, in this chapter, we will review some existing physics-based parametrizations relying on geometric and dynamic considerations of local wave properties. Pictorial representations of the wave breaking process relevant to this study are shown in Figures 1.1 and 1.2. There are many breaker models besides the ones discussed below, including the roller model [38], which makes extensive use of Duncan's [39,40] observations, or the eddy viscosity approach [41], but these will not be discussed here. First, following Duncan [39] and Phillips [42], energy dissipation in breakers is often expressed in terms of the dimensionless b parameter,

$$b = \frac{g\epsilon_l}{\rho c^5}, \tag{2.1}$$

owing, among other things, to its utility in expressing energy dissipation in a wave system as the fifth moment of Phillips' wave breaking distribution, $\Lambda(c)$. Here ε_l is the (dimensional) energy dissipation rate per unit length of breaking crest, c is the velocity of the breaking crest, ρ is the water density, and g is gravitational acceleration. The key observation is that the dissipation rates in geometrically similar breakers are proportional to the fifth power of the crest speed $c = |c|$. The dependence of the proportionality parameter b has seen several studies of its dependence on the breaker geometry since its introduction in Duncan [39].

One of the oldest approaches to characterizing breaker dissipation, particularly in shallow water, is to model breaking waves as being energetically equivalent to hydraulic jumps. The

dissipation rate of a hydraulic jump in shallow water is easily derived from applying a conservation analysis on the nonlinear shallow-water equations (NLSWEs) [43] and given by

$$\epsilon_l = \frac{\rho g}{4}\left(\frac{g(h_2 + h_b)}{2h_b h_2}\right)^{1/2}(h_2 - h_b)^3, \tag{2.2}$$

where h_b and h_2 are the water depth ahead of and behind the hydraulic jump, respectively. This model is, for example, used to set the energy dissipation in the "shock-capturing" approach of certain joint Boussinesq-NLSWE models [44], as well as in third-generation spectral wave models such as SWAN [45].

Inertial arguments for breaker properties have also been developed in deep [46] and shallow water [20] as a function of the breaker's geometric properties. They use the same dimensional analytical approach to develop their dissipation scaling arguments. The difference between them arises solely from the integral length scale of the eddies in the turbulent zone formed by the breaker (see Fig. 1.1). Namely, under Taylor's hypothesis, the local turbulent dissipation rate is given by $\varepsilon = u^3/l$: according to Mostert and Deike [20] and Drazen et al. [46], in both shallow and deep water, $u \approx \sqrt{2ga_b}$; in deep water $l \propto a_b$ [46], which reflects the length scale at which energy is input into the turbulent zone, while in shallow water $l \propto h_b$, since often $h_b \leq a_b$ and eddies with a diameter larger than the local depth cannot exist [20]. The dissipation rate per unit length of breaking crest is related to the turbulent dissipation rate by $\varepsilon_l = \rho A \varepsilon$, where the area of the turbulent zone is assumed to be cylindrical such that $A = \pi\, a_b^2\, /4$. This leads to the scalings

$$\epsilon_l = \beta_1 \rho g^{3/2} a_b^{5/2}, \quad b \propto S^{5/2} \tag{2.3}$$

in deep water, where S is the local slope parameter of the breaker [46], and

$$\frac{\epsilon_l}{\rho g^{3/2} h_0^{5/2}} = \beta_2 \left(\frac{a_b}{h_0}\right)^{7/2} \left(\frac{h_b}{h_0}\right)^{-1} \tag{2.4}$$

$$\epsilon_l = \beta_2 \rho g^{3/2} \frac{a_b^{7/2}}{h_b}, \quad b \propto (a_b/h_b)^{7/2} \tag{2.5}$$

in shallow water [20], where a_b is the wave amplitude at breaking and h_b is the water depth immediately ahead of the breaker, and β_1, β_2 are both dimensionless constants. Using appropriate semiempirical fits to draw together a variety of data sets [47], the deep-water model in particular has proved very successful for use in spectral wave modeling in the open ocean [47,48] and in its fundamental form has even been shown to perform slightly better than the hydraulic jump model in an inner surf zone problem (e.g., [49]). While very similar in formulation, the deep- and shallow-water models were applied to different environments. That is, the deep-water model of Drazen et al. [46] was applied to study dispersively focused wave packets, while the shallow-water model of Mostert and Deike [20] was applied to study shoaling solitary waves. Nevertheless, this approach is agnostic of the origin of the breaker of interest, as it considers only local geometric parameters at the point of breaking. These inertial models are what we will primarily compare in this study. Note that Pizzo et al. and Sinnis et al. [50,51] proposed a modification of the inertial model in Drazen et al. [46] for deep-water-focused packets by interpreting the cross-sectional area of the breaker in terms of a wave-number bandwidth. However, this work will not be directly

incorporated in the present study given the difficulty of defining wavelength [16] (or indeed bandwidth) for solitary waves. Finally, the model of Derakhti et al. [18] relays a dynamic criterion [52] for a breaking threshold, finding collapse of their breaker dissipation rates by using the semiempirical scaling, b = 0.034(Γ− 0.30)5/2, Γ= $T_b dB/dt|_{\mathrm{Bth}}$, where $B = u_x/c$ is the particle speed at the crest relative to the crest speed, $B_{\mathrm{th}} = 0.85$ is the threshold value of B taken as a criterion for breaking, and T_b is the period of the carrier wave. Although developed for breakers in deep and intermediate water, this model may also be applicable to shallow water or solitary waves; owing to difficulties in the measurement of Γ in the present data (see Section 4.5), we will not directly compare this parametrization.

Table 2.1 Values of $\Delta x/a_0$ for associated a_0/h_0

a_0/h_0	0.2	0.3	0.4	0.5
$\Delta x/a_0$	1/32.7	1/49.1	1/65.5	1/81.9

Chapter 3 Formulation and Methodology

3.1 Numerical Method

For the simulations used in this project, we use the Basilisk package to solve partial differential equations on regular adaptive Cartesian meshes [53]. The Basilisk package is an open-source numerical library, developed as a successor to the Gerris Flow Solver. Following [20], we use Basilisk to solve the nonlinear incompressible Navier-Stokes equations in two phases (air and water) with variable density and surface tension. In this solver, the Bell-Colella-Graz projection method [54] issued to solve the momentum equation, and a momentum-conservative volume of fluid (VOF) advection scheme is used to advect the liquid-gas boundary, which helps to maintain a relatively sharp interface representation [55]. The method in Brackbill et al. [56], which was further developed and implemented by Popinet [55], is used to model the surface tension.

The incompressible Navier-Stokes equations with surface tension and variable density govern the flow in two phases (water and air) and can be written as

$$\begin{cases} \rho(\partial_t \boldsymbol{u} + (\boldsymbol{u}\cdot\nabla)\boldsymbol{u}) = -\nabla p + \nabla\cdot(2\mu\boldsymbol{D}) + \gamma\kappa\delta_s\boldsymbol{n} \\ \partial_t\rho + \nabla\cdot(\rho\boldsymbol{u}) = 0 \\ \nabla\cdot\boldsymbol{u} = 0 \\ \frac{\partial f}{\partial t} + \boldsymbol{u}\cdot\nabla f = 0 \end{cases}, \tag{3.1}$$

where $u = (u, v)$ is the fluid velocity, ρ the density, μ the dynamic viscosity, and D the deformation tensor. The interface between air and water is defined by the $\gamma\kappa\delta_s n$ term, where δ_s is the Dirac delta function, γ is surface tension, and κ and n are the mean curvature and normal of the interface, respectively, which are estimated using a height function approach in the VOF scheme [55]. The

volume of fluid tracer f is used to distinguish between air and water phases and sets the density and viscosity in the relevant phase.

The Basilisk software library features a quadtree-based adaptive mesh refinement (AMR) scheme, which allows highly effective resolutions to be attained at a fraction of computational cost associated with conventional, uniform-grid approaches [53,57]. The method identifies and finely resolves only the active portions of the simulated flow, while using coarser local resolutions for roughly quiescent regions. In particular, the AMR approach more easily allows the direct resolution of small-scale turbulence in water without the need of a turbulence model. The criterion for refinement is determined through a wavelet algorithm, which estimates the discretization error in the velocity and VOF fields, following [20,35].

In this project, effective resolutions are stated in terms of the level parameter Le, where $x = L_0/(2^{Le})$ is the minimum grid size and L_0 is the domain length. The maximum resolution is set to Le = 13 for the cases presented here; numerical convergence of the energy budgets, which are used to determine energy dissipation, is shown in Appendix A.

For all simulations, the bathymetry length was set to $L_0/h_0 = 50$. We have $\Delta x/L_0 = 1/2^{13}$ and $\Delta x/Lc = 1/1638.4$, where $Lc = 10h_0$. For the viscous boundary layer, we use Batchelor's estimate, $\delta v \sim h_0/\sqrt{Re} = 5 \times 10^{-3}h_0$. Therefore, $\Delta x/\delta_v = 1/(5 \times 10^{-3}h_0)$. For the capillary length scale, we have $\Delta x/\lambda_c = 3.67$ cm^{-1} (although for this 2D study we do not consider bubbles or droplets). Additionally, several values of $\Delta x/a_0$ are shown in Table 2.1 for various values of a_0/h_0. The maximum resolution is 16 cells over the wave amplitude.

3.2 Problem Formulation

In this project, we consider a varying bathymetry, featuring a depth change with a linear transition, as illustrated in Figure 1.2, as a simple model for wave runup in storm surge conditions. After some distance, *Lc*, the bathymetry changes from a uniform flatness (hereafter offshore region) to a uniform slope. This slope continues until the storm surge depth h_s is reached, upon which the bathymetry returns to a uniform flatness (hereafter inshore region) for the rest of the domain, representing the storm surge area. We set the problem by considering a solitary wave of amplitude a_0, traveling in the x direction over a uniform water depth of h_0, as illustrated in Figure 1.2. A negative storm surge depth h_s corresponds to an inshore region elevated above the undisturbed water level. The wave may break either over the sloped transition or over the inshore region. The latter case can occur only for positive inshore depths h_s, while the former case can occur for h_s of any sign.

We use the depth h_0 to set the length scale. We set a reference velocity scale using the linear speed $c_0 = \sqrt{gh_0}$ and find the solitary wave phase speed to be $c/c_0 = \sqrt{1 + a_0 h_0}$. The timescale is then set as $t_0 = \sqrt{h_0/g}$. We use the Bond number, Bo = $\rho g h_0^2 / \sigma$ = 1000, to set the surface tension, and the Reynolds number, Re = $c_0 h_0 / \nu$ = 40000, to set the water kinematic viscosity. A ratio of air density to water density (ρ_{air}/ρ) of 1/850 is used. The chosen value of Re corresponds with a depth of h_0 = 5.46 cm, and Bo with a depth of 8.6 cm for water and air at room temperature. Following evidence from studies of short (deep-water) waves [33–35], we expect these values of Re and Bo to be asymptotically large, and thus the essential dynamics of the wave propagation and breaking problem are insensitive to them. Specifically, we expect the speed and rate of wave steepening to be insensitive to Re and Bo, consistent with the findings of Mostert and Deike [20], who validated their numerical data partly against the experiments of Camfield and Street [11,12],

which were run at different values of these parameters. The shape of the overturning wave and the local turbulent dissipation rate is also expected to remain insensitive to these values, given observations in deep water [33–35]. To keep the numerical simulations tractable, we therefore do not vary these parameters in the present study, but this assumption remains to be confirmed for shallow-water contexts in future work.

The wave is initialized using the exact soliton solution to the Green-Naghdi equations [58] given by

$$\eta(x) = a_0 \mathrm{sech}^2\left[(x - x_w)\sqrt{\frac{3a_0}{4h_0^3}\left(\frac{1+a_0}{h_0}\right)}\right] \tag{3.2}$$

$$u_x(x) = \frac{c\eta(x)}{h_0 + \eta(x)}, \quad u_y(x,y) = \frac{c(y+h_0)}{h_0+\eta(x)}\frac{\partial \eta}{\partial x}\left(1 - \frac{\eta}{h_0+\eta_0}\right) \tag{3.3}$$

This forms a solitary wave, at location x_w in Figure 1.2, that propagates inshore towards the beach, steepens, and breaks, as described in Section 4.1.

In this project, 123 cases are simulated by varying the three parameters, which are the storm surge depth h_s, the beach slope $\alpha \equiv \tan\theta$, and the offshore wave amplitude a_0, as illustrated in Table 3.1. For each combination of initial wave amplitude and beach slope, cases are run covering inshore depths from $h_s/h_0 = -0.4$ to 0.5. Cases with negative storm surge depths represent bathymetry where the inshore region is above the water initially, causing the wave to break against the beach slope. This case is somewhat similar to the bathymetry condition considered in [20], which could be interpreted as the limiting case $h_s/h_0 \to -\infty$.

Table 3.1 Outline of the simulated cases. The varying parameters are the beach slope $\alpha \equiv \tan\theta$ (rows) and offshore wave amplitude a_0 (columns). Note that the beach slope ranges fall under the small angle approximation, $\alpha \approx \theta$. The individual entries mark the number of different storm surge (inshore) depths that have been run for the corresponding values of a_0, θ; these vary from $h_s/h_0 = -0.4$ to 0.5.

θ \ a_0/h_0	0.2	0.3	0.4	0.5
2°	7	8	8	8
3°	7	8	8	8
4°	7	8	8	7
5°	7	8	8	8

Chapter 4 Results and Discussion

4.1 Describing the Wave-breaking Process

This chapter discusses the wave breaking process for some representative cases, in which different types of breakers are formed, as illustrated in Figures 4.1–4.3. Figure 4.1 presents the vorticity around the wave in water at four representative time instants during wave breaking for a case with a positive storm surge depth. For this case the beach slope is $\theta = 4^{\circ}$, the initial wave amplitude is $a_0/h_0 = 0.4$, and the storm surge (inshore) depth is $h_s/h_0 = 0.2$. The wave begins to break around the boundary between the uniform slope and inshore region (see Fig. 4.1(a)); as the wave propagates further, an air cavity forms inside the breaker (see Fig. 4.1(d)), which is characteristic of a plunging breaker. An additional plunging breaker with a negative storm surge depth is described in Appendix B (see Fig. B.1).

Figure 4.2 shows a case with a large storm surge depth. Here the beach slope is $\theta = 3^{\circ}$, the initial wave amplitude is $a_0/h_0 = 0.3$, and the storm surge depth is $h_s/h_0 = 0.5$. Similar to Fig. 4.1, the wave breaks on the inshore region, but no clear air cavity is encapsulated as the wave breaks, making this is a spilling breaker. Finally, Figure 4.3 shows a case with a large beach slope. Here the beach slope is $\theta = 5^{\circ}$, the initial wave amplitude is $a_0/h_0 = 0.4$, and the storm surge depth is $h_s/h_0 = -0.4$, i.e., the inshore region lies well above the undisturbed water level. The wave breaks on the beach slope. From Figure 4.3(d), an air pocket is observed, indicating that a plunging breaker is formed.

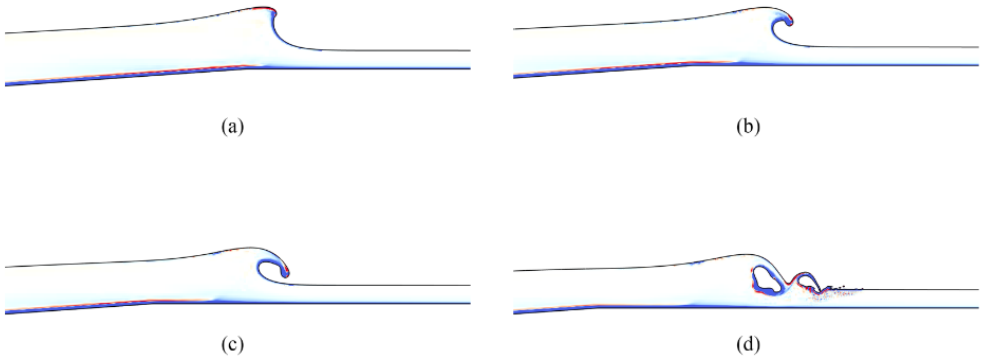

Figure 4.1 Wave breaking process (plunging breaker) for the case with a beach slope of 4◦, initial wave amplitude of 0.4, and storm surge depth of 0.2. Vorticity (color contour) in the water phase at the following four time instants: (a) t/t_0 = 13.8, (b) t/t_0 = 14.4, (c) t/t_0 = 14.7, (d) t/t_0 = 15.3.

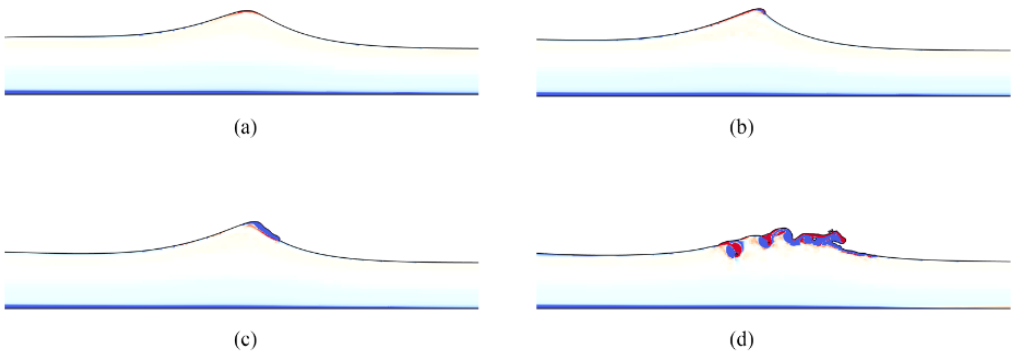

Figure 4.2 Wave breaking process (spilling breaker) for the case with a beach slope of 3◦, initial wave amplitude of 0.3, and storm surge depth of 0.5. Vorticity (color contour) in the water phase at the following four time instants: (a) t/t_0 = 19.75, (b) t/t_0 = 21.75, (c) t/t_0 = 23.2, and (d) t/t_0 = 26.0.

In summary, plunging breakers exhibit clear overturning jets, such as those visible in Figures 4.1(b), 4.1(c), 4.3(b), 4.3(c), and B.1(c); although spilling breakers also feature overturning behavior, which is essentially the same process as in plungers on smaller length scales [16,33,59], and is not easily distinguishable in the present simulations.

4.2 Classifying the Types of Breakers for All Simulation Cases

The breakers for all simulation cases are classified as either plunging breakers or spilling breakers. Plunging breakers are characterized by the presence of a well-defined cavity underneath the overturning jet, while spilling breakers in this data set correspond to any other breaking morphology. We note that there is no fundamental difference between plunging and spilling breakers. New et al. [60] observed that spilling breakers overturned in a remarkably similar manner to plunging breakers, where the scale of the overturning jet is merely smaller. The same phenomenon was observed in the context of solitary waves specifically [16]. The similarity does break down for sufficiently small wavelengths, in which case parasitic capillary waves can arise and modify the breaking process [33,61], but this phenomenon occurs for Bond numbers significantly smaller than those considered in the present study and is not qualitatively apparent in our simulations. Nevertheless, plunging breakers as we have defined them here are known to cause significantly increased loadings on offshore structures owing to the presence of the entrained air cavity [62], and the entrained cavity can also affect the wave's dissipative properties [34,35]. It therefore remains of interest to identify this broad change in wave character.

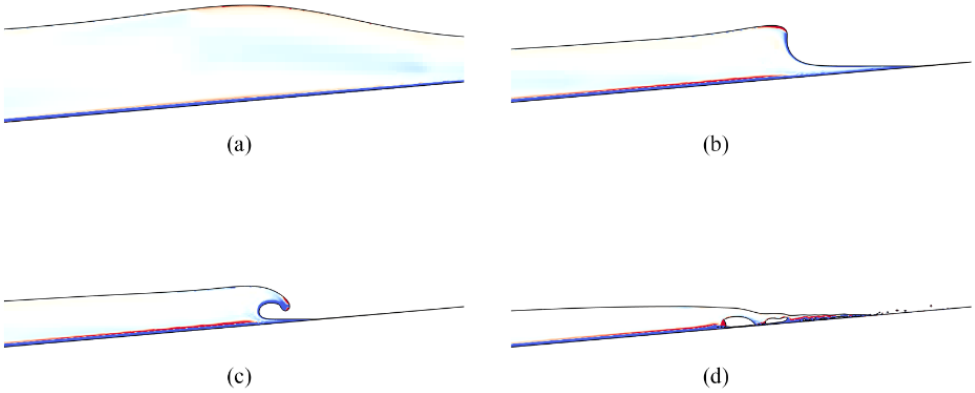

Figure 4.3 Wave breaking process (plunging breaker) for the case with a beach slope of 5°, initial wave amplitude of 0.4, and storm surge depth of −0.4. Vorticity (color contour) in the water phase at the following four time instants: (a) $t/t_0 = 7.25$, (b) $t/t_0 = 12.25$, (c) $t/t_0 = 13.2$, and (d) $t/t_0 = 14.45$.

To determine whether the type of breaker can be determined by the local conditions of the wave at the moment of breaking, the wave amplitude at breaking a_b and water depth h_b under the breaking wave is extracted from the data for each case and normalized by h_0 to get dimensionless wave amplitude a_b/h_0 and water depth h_b/h_0. The breaking amplitude is then plotted against breaking depth (a_b/h_0, h_b/h_0), as shown in Figure 4.4, with solid and hollow markers denoting spilling and plunging breakers, respectively. The shape of the marker denotes the beach slope. The solid markers and the hollow markers can be separated by a line, which is governed by $h_b = a_b - 0.12$ (*i.e.*, $a_b/h_b \approx$ const) as indicated by the dashed line in Figure 4.4. Given that plunging and spilling breakers are governed by the same overturning behavior, though at different length scales [16,33,59], the particular form of this separating line does not reflect a change in fundamental physical processes, but may instead suggest that breaker intensity correlates with the so-called breaking index $\gamma \equiv a_b/h_b$, which is equivalent to one form of the nonlinearity parameter F (see Section 4.4). Further, Figure 4.4 suggests that (1) breaking amplitude and depth are rather

insensitive to beach slope, and (2) for a given breaking depth, plunging breakers have larger amplitudes than spilling breakers. In other words, if the wave amplitude at breaking is relatively larger, it will have a higher chance to encapsulate air and thus will more likely form a plunging breaker. (3) For sufficiently low wave amplitude and sufficiently high depth, a wave will not break, as indicated by the solid black markers. This threshold is suggested by Losada et al. to be a_b/h_b = 0.7, for example [21].

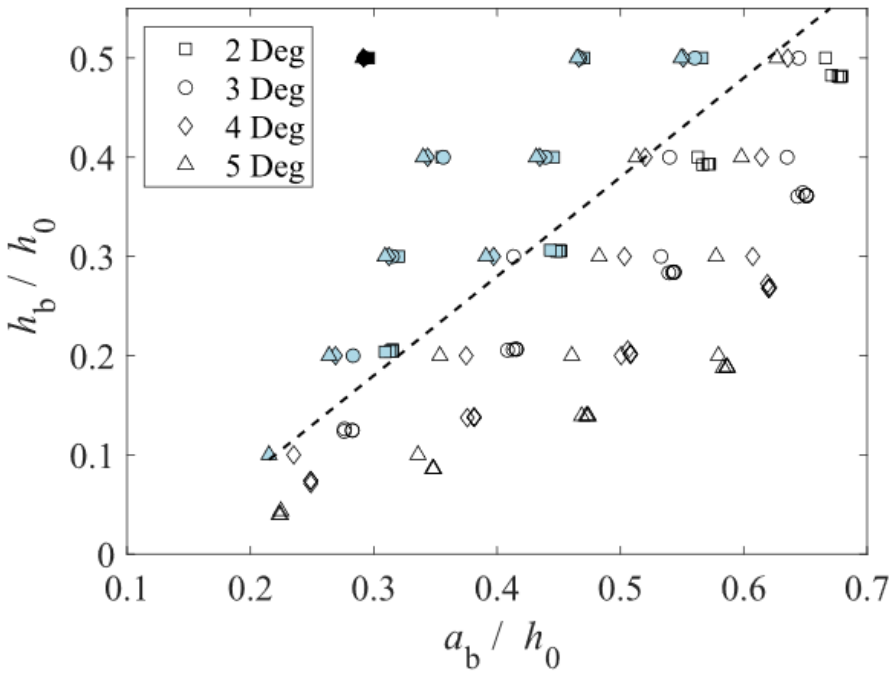

Figure 4.4 Breaker types of all simulated cases. Blue-filled shapes represent spilling breakers, and hollow shapes represent plunging breakers. Black-filled shapes at locations of maximum local wave height represent nonbreaking cases. The dashed line ($h_b = a_b - 0.12$) separates the spilling breaking cases from the plunging breaking cases.

4.3 Determining Energy Budget and Dissipation

For all the simulated cases, the energy dissipation is examined. Figure 4.5 shows the energy dissipation process for a few representative cases, namely, with storm surge (inshore) depths of $h_s/h_0 = -0.2$, 0.1, 0.3, and −0.4, respectively.

In the figures, the dotted line represents the gravitational potential energy, the dashed line represents the kinetic energy, and the dark line represents the sum of these two, as the total conservative energy. The surface tension energy has been found in such cases to be negligible [20,33]. The leftmost vertical line represents the time when the wave begins to break (namely, when the wave face becomes vertical). The natural end time of breaking, however, is not immediately obvious. In Mostert and Deike [20] the end time was defined as the moment after breaking that the gravitational potential and kinetic energies were equal; this corresponds to the crossover of these energies in the case of Figure 4.5(a), which has a negative storm surge depth and thus the wave breaks on the beach slope. This is due to the transfer of kinetic energy to gravitational potential energy as the wave runs up the beach. In such a case, the wave exchanges kinetic energy that would otherwise be available for dissipation through breaking into gravitational potential energy, which rapidly slows or terminates the breaking process. However, such a moment does not arise naturally for cases with positive storm surge depths or for small negative storm surge depths in the present study. This is because for such cases, the breaker cannot gain a significant amount of gravitational potential through runup; it thus retains kinetic energy available for dissipation, allowing the breaking process to prolong without a clear endpoint. Therefore, in this project, an approach to determining the breaking end time is developed using a linear regression of the total energy budget, as shown in Figure 4.5. First, in our analysis, we consider a parameter sweep to be a series of cases of varying storm surge depths ($h_s/h_0 = -0.4$–0.5) with the same

combination of beach slope (θ) and initial wave amplitude (a_0), as shown in Table 3.1. For each combination of (a_0/h_0, θ, h_s /h_0), a least-squares line is fit to the energy budget from the breaking time $t_1 = t_b$ to a range of candidates for the end time t_2. The candidate of t_2 resulting in the best fit (i.e., with the highest determination coefficient R^2) is noted. For a given combination of (a_0/h_0, θ), the results are then averaged into a single end breaking time, across the set of all corresponding storm surge depths. The range of best end breaking times within this set is used to develop error bars for the dissipation rate at each storm surge depth. While all the cases at a given (a_0/h_0, θ) share the same temporal distance between the start and end of breaking, each case will have distinct error bars for energy dissipation rate since the energy budget is unique for each case.

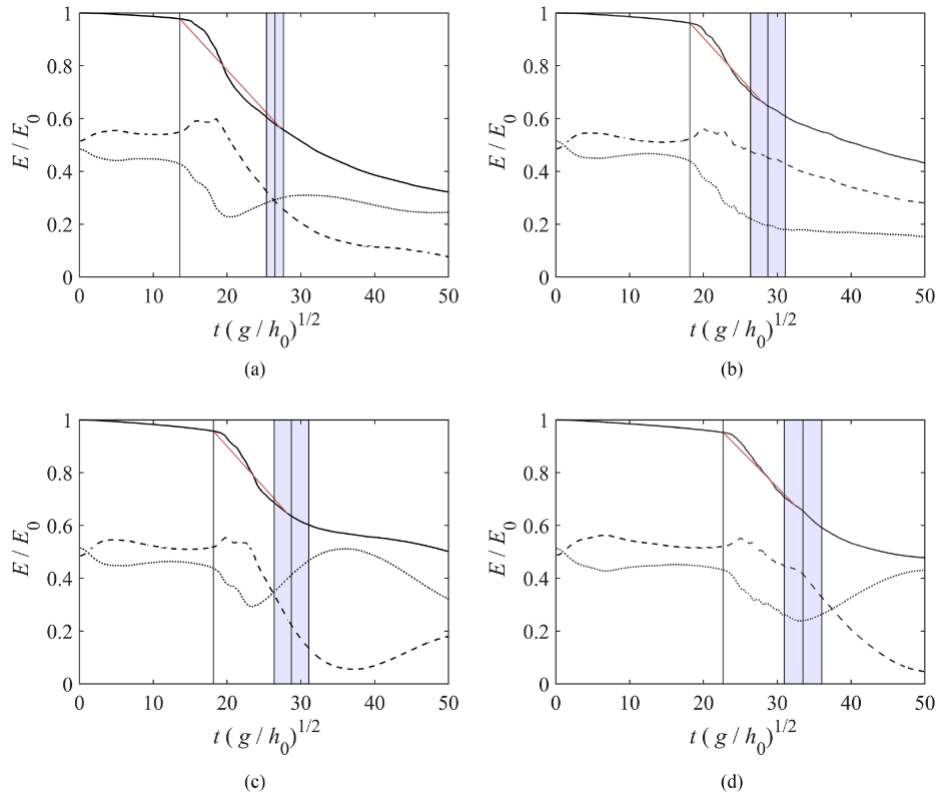

Figure 4.5 Energy dissipation for representative cases: (a) 0.5 amplitude, 3˚ beach slope, −0.2stormsurge depth; (b) 0.3 amplitude, 3˚ beach slope, 0.1 storm surge depth; (c) 0.3 amplitude, 3˚ beach slope, −0.4 storm surge depth; and (d) 0.3 amplitude, 2˚ beach slope, −0.4 storm surge depth. Kinetic energy is shown as the dashed line, gravitational potential energy is shown as the dotted line, and total energy is shown as the solid line. The leftmost vertical line represents the start of breaking time, while the three rightmost vertical lines represent the error bar approximation of breaking end time. The solid red line represents the line of best fit for the specific total energy dissipation curve.

Results for some representative cases are shown in Figure 4.5. The red line in each figure shows a linear fit between $t_1 = t_b$ and the candidate t_2 with the highest R^2 value for that case; the three rightmost vertical lines in the shaded region represent the end time of the breaking event with the center line representing the average breaking end time across all storm surge depths at the given (a_0/h_0, θ), and the left and right lines representing the error bar range. From all figures, a clear drop in total energy is observed as the wave breaks. The cases with negative storm surge depths show a steep drop in kinetic energy when compared to those with positive storm surge

depths, due to wave breaking on the beach slope, which reduces the water velocity more significantly. For all cases, the initial energy dissipation observed in the wave before breaking is a physical effect captured by the numerical simulations and is numerically converged in our study. Figure 7(a) shows that for negative storm surge depths, this method can predict a breaking end time very close to the crossover point between kinetic and gravitational potential energy used in Mostert and Deike [20], without any additional tuning of parameters, although we note that this behavior is not observed in all cases. While the kinetic or gravitational crossover often lies within the range of best t_2 within a given set of storm surge depths, as in Figure 4.5(c), this is not always guaranteed (see Fig. 4.5(d)).

4.4 Characterizing Dissipation Rate

The energy dissipation induced by a breaking wave is typically described by its dissipation rate per unit length of breaking crest, ε_l [39]. In this project the dissipation rate is determined using a linear fit to the total energy (i.e., the sum of gravitational potential and kinetic energies) during the breaking event,

$$\epsilon_l = \frac{\Delta E}{\Delta t}, \tag{4.1}$$

where $\Delta E = |E_1 - E_2|$ and $\Delta t = |t_1 - t_2|$, with subscripts 1 and 2 representing the start and end of the breaking event, respectively. Aside from how t_2 is determined (see Section 4.3), this is consistent with the methodology applied in [20,35]. The dissipation rates for all simulation cases are shown in Figure 4.6.

Figure 4.6(a) plots the dissipation rates against normalized ab for all the simulated cases. The colors of black, red, green, and blue represent beach slopes of $\theta = 2^{\circ}$, 3°, 4°, and 5°, respectively. Scaled dissipation rate is plotted with respect to the local breaking conditions, where the constant, $\varepsilon_0 = \rho g^{3/2} h_0^{5/2}$, is used to normalize the dissipation rate. Error bars are included for each data point to calculate the dissipation rate at the upper and lower limits of the end breaking time as described in Section 4.3. The dissipation rate from Mostert and Deike [20] is shown as hollow squares in Figure 4.6(a) for comparison. In general, across all cases the dissipation rate increases with the wave amplitude at breaking, but there is considerable variation in the data due to the effects of the beach slope and inshore storm surge depth. Note that despite the methodological differences, the estimates for the dissipation rate for negative storm surge depths in the present data lie approximately within the spread of the cited data from Mostert and Deike [20], which corresponds to the limit $h_s/h_0 \rightarrow -\infty$.

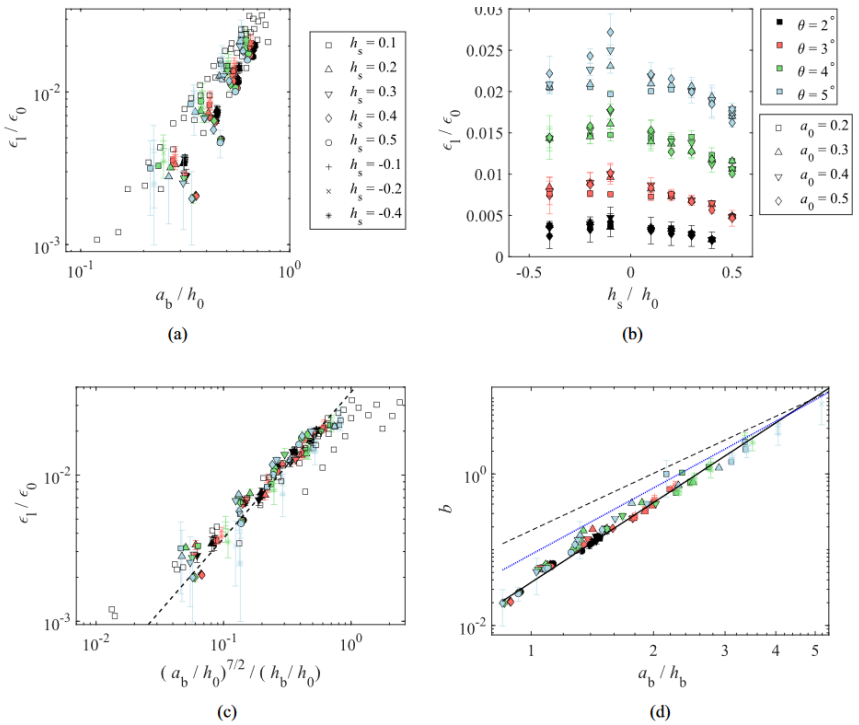

Figure 4.6 (a) Dissipation rate plotted against normalized wave amplitude at breaking for all simulated cases. Data from Mostert and Deike [20] are also included as hollow squares for comparison. (b) Dissipation rate plotted against storm surge depth. (c) Dissipation rate plotted against a_b scaled by h_b. The line represents the shallow water inertial model from [20]. (d) Breaking parameter shown in Eq. (2.1) plotted against nonlinearity parameter a_b / h_b. Dashed and solid lines represent deep- and shallow-water scalings, respectively. Blue dotted line represents the hydraulic jump bore model [43]. For panels (c) and (d), shape representation is as shown in (a), and for all panels, color representation is as shown in panel (b).

Figure 4.6(b) shows the dissipation rate plotted against storm surge depth for all simulation cases. Clear delineations can be seen between the cases of the various beach slopes. The cases with higher beach slopes tend to experience a higher dissipation rate. Overall, for the cases with positive storm surge depths, the dissipation rate decreases with increasing storm surge depth. This is because for positive h_s / h_0, the wave can break either on the slope ($h_b > h_s$) or on the inshore region ($h_b = h_s$); hence, following the inertial argument of Chapter 2, the integral length scales of the turbulence can only increase with increasing h_s / h_0, corresponding with lower dissipation rates. On the other hand, for the cases with negative storm surge depths, dissipation rate decreases with

increasing $|h_s/h_0|$, i.e., with an increasing elevation difference between the inshore region and the undisturbed water level, the greatest energy dissipation rate occurs where the inshore region is at an elevation only slightly higher than the water level. While all waves with negative h_s/h_0 break on the sloped region, the resulting runup forces the integral length scales of the turbulent flow to reduce, driving an increase in dissipation rate. This effect is strong for small values of $|h_s/h_0|$. However, for large negative values of h_s/h_0, the breaker runs up the slope and thereby rapidly exchanges kinetic energy for gravitational potential energy, so that there is less available energy for dissipation. This effect appears to outstrip the increase in dissipation rate resulting from the smaller integral length scales and results in a lower dissipation rate. Note finally that the negative values of h_s/h_0 tend to show slightly larger error bars than positive h_s/h_0; these indicate greater variability in the energy budget between different slopes and wave amplitudes for a given storm surge depth.

We now examine the performance of different parametrizations in capturing the trends in the data. Figure 4.6(c) shows the energy dissipation rates scaled according to Equation (2.5), i.e., the shallow-water parametrization of Mostert and Deike [20]. The data collapse consistently with the scaling, represented by the dashed line in the figure. For small dissipation rates and high beach slopes, the data with negative h_s/h_0 values tend to show the greatest relative deviation from the scaling (in addition to having large error bars). This reflects that as the wave runs up the beach, the inertial argument that leads to Equation (2.5) becomes less relevant because the breaking depth h_b is no longer properly defined. Moreover, as the breaker runs up the beach, dissipation due to the bottom boundary layer may become significant; such effects are not accounted for in Equation (2.5). These observations also apply to the DNS data of Mostert and Deike [20] and may explain why it does not fully collapse to the parametrization.

We compare other parametrizations in Figure 4.6 (d), making use of the nonlinearity parameter of Beji [63],

$$F = \frac{ga^2}{c^2}, \tag{4.2}$$

where a is a representative amplitude and c is a phase speed. In the shallow-water limit, with $c = \sqrt{gh_b}$, we have $F \rightarrow a_b/h_b$. We also explicitly use the dimensionless breaking parameter b defined in Equation (2.1), which is especially relevant to deep-water studies [39,46], but can also be defined for shallow water (see Chapter 2). With $c = \sqrt{gh_b}$, the shallow water scaling (Eq. (2.5) of Mostert and Deike [20]) can be nondimensionalized into $b \propto F^{7/2}$ and is shown with a solid line. In the deep-water limit (i.e., the context of Drazen et al. [46]), $F \rightarrow S$ where S is the breaking slope, and obtains $b \propto F^{5/2}$. Note that the inertial argument of Drazen et al. [46] can apply to any breaker, provided the integral length scale of the turbulence can be approximated by a_b (rather than h_b, as in Mostert and Deike [20]), which could occur in the shallow-water limit for cases where $a_b/h_b \geq 1$, which is common in the present data. Even in this case, however, the scaling $b \propto F^{5/2}$ is recovered. This is shown by the dashed line. Finally, the dimensionless form of the bore model (2) yields

$$b = \beta F^3 \left(\frac{2+F}{2+2F} \right)^{1/2} \tag{4.3}$$

and is shown with the blue dotted line. This model relies on the assumption that all waves in shallow water can be energetically modeled as hydraulic jumps. When plotted together, the data obtained in this project appear to best match the inertial scaling in Eq. (2.5) of Mostert and Deike [20]. The other scalings have shallower slopes, with the deepwater scaling deviating most from the data obtained in this project.

4.5 Considerations for a General Breaking Parametrization

We have found that for solitary waves in the presence of a simple storm surge geometry, the shallow-water parametrization $b \propto F^{7/2}$ of Mostert and Deike [20] accurately predicts the dissipation rate of breaking. It better collapses the DNS data of the present study than for the hydraulic jump model, Eq. (2.2), suggesting that solitary waves are not well approximated energetically by hydraulic jumps. However, the shallow-water parametrization $F^{7/2}$ performs better even for breakers where $a_b > h_b$, equivalently $F > 1$, for which one might expect that the parametrization $b \propto F^{5/2}$ of [46] would be superior. We therefore discuss whether these two parametrizations could be harmonized across different data sets, including both shallow- and deep-water regimes.

Note the nonlinearity parameter F in Eq. (4.2) can be used to nondimensionalize the water wave equations in a depth-independent way. Using the linear phase speed in arbitrary depth, $c_2 = (g/k) \tanh(kh)$, in the short-wave (deep-water) limit, $F \sim ak = S$ is the wave slope, while in the long-wave (shallow-water) limit, $F \sim a/h$. Figure 4.7(a) shows the b parameter for a variety of experimental and numerical sources for deep-water breakers [33,34,46,64,65], along with the present shallow-water data set. While the shallow-water data set appears to have a slope

qualitatively similar to the deep-water data, there is a clear break between the two groups, and a single power-law scaling cannot capture both data sets.

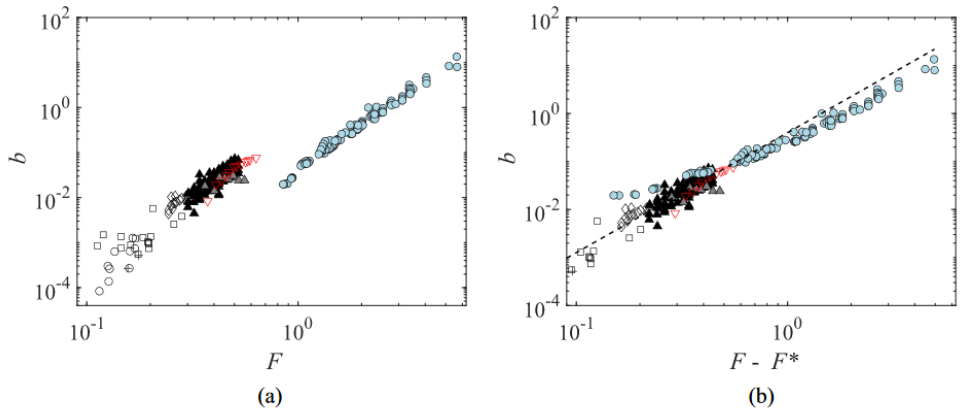

Figure 4.7 (a) Plot of b parameter against nonlinearity parameter F for shallow-water data from the present study and deep-water data from literature. Black and gray triangles and gray diamonds are from Drazen et al. [46]; cross and circles from Banner and Peirson [64]; squares from Grare et al. [65]; red triangles are DNS from Deike et al. [33]. Blue circles are the present shallow-water DNS. (a) Data plotted without shifts or scaling, (b) Data shifted horizontally by estimated breaking threshold F^*. For the deep-water data, $F^* = 0.08$; for the present shallow-water DNS data, $F^* = 0.7$.

The difference may possibly be accommodated with a heuristic consideration of breaking threshold. In their semiempirical study, [47] fitted a best-fit curve to deep-water data, finding

$$b = 0.4(S - S_T)^{5/2} \tag{4.4}$$

with $S_T = 0.08$. Here ST can be qualitatively interpreted as a breaking threshold, which is closely related to questions of breaking dissipation. Identifying breaking criteria in deep and shallow water remains an active research topic [33,46,50–52,66–68], and recent investigations have shown that

the breaking criterion in deep water depends on the bandwidth of the breaking wave group, somewhat equivalent to a Benjamin-Feir index [50,51,68]. It is not the purpose of this study to speculate on the breaking threshold for shoaling solitary waves, and breaker bandwidth is not well defined for these waves, but we may give a rough heuristic estimate of $F^* \approx 0.7$, following Losada et al. [21] who found this threshold for solitary waves encountering abrupt depth changes. Plotting a modified fit of $b = 0.4(F - F^*)^{5/2}$ with $F^* = 0.08$ in deep water, and $F^* = 0.7$ in shallow water, produces Figure 4.7(b), which more closely collapses the deep- and shallow-water data.

While promising, the above approach, and indeed the comparison of different parametrizations in Section 4.4, essentially sets $F = a_b/h_b$, well known as the breaking index γ [69], but it relies on identifying the crest speed with the linear wave speed at the breaking depth, $c = \sqrt{g h_b}$. However, the breaking crest remains close to its offshore speed, $c_0 = \sqrt{g(h_0 + a_0)} \approx \sqrt{g h_b}$, which is a more natural choice for nondimensionalizing the energy dissipation. Using it identifies the b parameter with the left-hand side of Equation (2.4), since $g^{3/2} h_0^{5/2} = c_0^5/g$, in which case we can interpret Equation (2.4) as

$$b_0 = \beta F_0^{7/2} M^2 = \beta F_0^{5/2} \gamma \tag{4.5}$$

where $b_0 = g\varepsilon/(\rho c_0^5)$, $F_0 = a_b/h_0$, and $M^2 = c_0/c = h_0/h_b$ is the ratio of the inshore and offshore wave speeds, and γ is the breaking index. The second half of Equation (4.5) is suggestive of a close link with the deep-water scaling [46], except that γ (and M^2) do not have deep-water equivalents, so they cannot be immediately compared on the same axes.

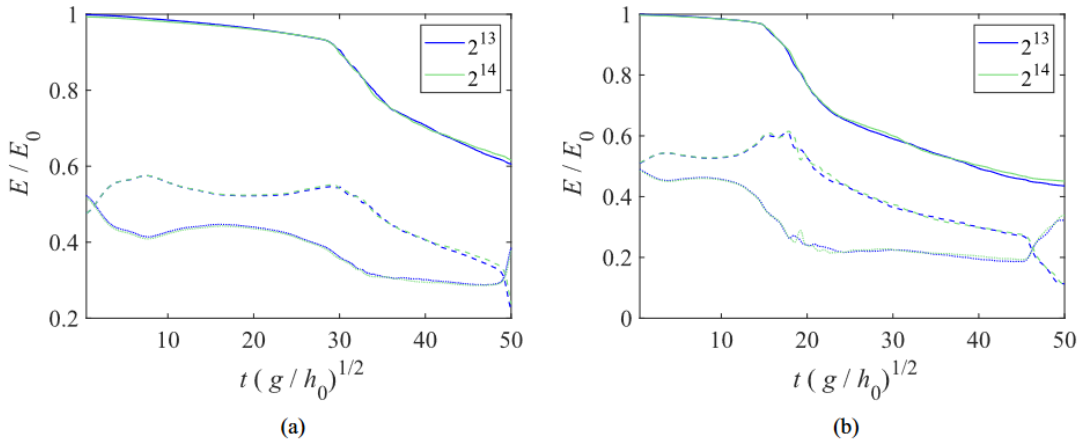

Figure 4.8 Comparison of energy budget between two mesh resolution levels 213 and 214 for two cases: (a) 0.2 initial wave amplitude, 2˚ beach slope, and 0.3 storm surge depth; (b) 0.4 initial wave amplitude, 4˚ beach slope, and 0.3 storm surge depth.

We remark finally that the dynamic/kinematic parametrization of [18] using the parameter Γ has shown good data collapse, but Γ is difficult to estimate for the present data owing to noise in the numerical differentiation of the related quantity u_x/c, evaluated at the wave crest.

Chapter 5 Conclusions

In this project, we have conducted various two-dimensional direct-numerical simulations of solitary wave breaking over a simple storm surge bathymetry, varying the depth of the storm surge, beach slope, and wave initial amplitude. The resulting breakers can be classified into plunging or spilling breakers through a clear separation line, which was developed based on wave amplitude and water depth at the point of breaking. In addition, we studied the energy dissipation of the cases to determine a dissipation rate for each case. After comparing with prior dissipation rate data from the literature, we found that the shallow water dissipation rate model developed in Mostert and Deike [20] can be extended to this storm-surge-style bathymetry with good data collapse, performing better than the hydraulic jump analogy or the deep-water parametrization of Drazen et al. [46]. Furthermore, we compared our shallow water data with deep water data from literature using a breaking parameter and explored possibilities of a unifying model. A promising collapse of most of the data can be obtained. The obtained results from this project could be used in the future to study how changes in the energy dissipation of breaking waves affect the wave loading on coastal structures, particularly in the presence of a storm surge. Possibilities for implementing the parametrization of Mostert and Deike [20] into a Boussinesq-type or other regional-scale wave-resolving model will also be explored in a future study. In addition, the obtained parameterization will be used in the related larger-scale Boussinesq model to obtain the combined wind-surge-wave loading for bridges in coastal regions.

References

1. Elko, N., Feddersen, F., Foster, D., Hapke, C., McNinch, J., Mulligan, R., ... & Raubenheimer, B. (2015). The future of nearshore processes research. *Shore Beach*, *83*(1), 13.

2. Melville, W. K. (1996). The role of surface-wave breaking in air-sea interaction. *Annual review of fluid mechanics*, *28*(1), 279-321.

3. Battjes, J. A. (1988). Surf-zone dynamics. *Annual Review of Fluid Mechanics*, *20*(1), 257-291.

4. Feddersen, F., & Trowbridge, J. H. (2005). The effect of wave breaking on surf-zone turbulence and alongshore currents: A modeling study. *Journal of Physical Oceanography*, *35*(11), 2187-2203.

5. Moulton, M., Suanda, S. H., Garwood, J. C., Kumar, N., Fewings, M. R., & Pringle, J. M. (2023). Exchange of plankton, pollutants, and particles across the nearshore region. *Annual Review of Marine Science*, *15*, 167-202.

6. US Army Corps of Engineers. (2002). Coastal engineering manual. *US Army Corps of Engineers, Engineer Manual 1110-2-1100*.

7. Wu, X., Feddersen, F., & Giddings, S. N. (2021). Diagnosing surfzone impacts on inner-shelf flow spatial variability using realistic model experiments with and without surface gravity waves. *Journal of Physical Oceanography*, *51*(8), 2505-2515.

8. Guza, R. T., & Feddersen, F. (2012). Effect of wave frequency and directional spread on shoreline runup. *Geophysical Research Letters*, *39*(11).

9. Feddersen, F. (2012). Observations of the surf-zone turbulent dissipation rate. *Journal of Physical Oceanography*, *42*(3), 386-399.

10. Bautista, E. G., Arcos, E., & Bautista, O. E. (2011). Propagation of ocean waves over a shelf with linear transition. *Mecánica Computacional*, *30*(4), 225-242.

11. Camfield, F. E., & Street, R. L. (1969). The effects of bottom configuration on the deformation, breaking and run-up of solitary waves. In *Coastal Engineering 1968* (pp.173-189).

12. Camfield, F. E., & Street, R. L. (1969). Shoaling of solitary waves on small slopes. *Journal of the Waterways and Harbors Division*, *95*(1), 1-22.

13. Synolakis, C. E. (1987). The runup of solitary waves. *Journal of Fluid Mechanics*, *185*, 523-545.

14. Skjelbreia, J. (1987). *Observation of breaking waves on beaches by use of an LDV* (Doctoral dissertation, PhD thesis, California Institute of Technology).

15. Grilli, S. T., Losada, M. A., & Martin, F. (1994). Characteristics of solitary wave breaking induced by breakwaters. *Journal of Waterway, Port, Coastal, and Ocean Engineering*, *120*(1), 74-92.

16. Grilli, S. T., Svendsen, I. A., & Subramanya, R. (1997). Breaking criterion and characteristics for solitary waves on slopes. *Journal of waterway, port, coastal, and ocean engineering*, *123*(3), 102-112.

17. Li, Y., & Raichlen, F. (2002). Non-breaking and breaking solitary wave run-up. *Journal of Fluid Mechanics*, *456*, 295-318.

18. Derakhti, M., Banner, M. L., & Kirby, J. T. (2018). Predicting the breaking strength of gravity water waves in deep and intermediate depth. *Journal of Fluid Mechanics*, *848*, R2.

19. Grilli, S. T., Horrillo, J., & Guignard, S. (2020). Fully nonlinear potential flow simulations of wave shoaling over slopes: Spilling breaker model and integral wave properties. *Water Waves*, *2*(2), 263-297.

20. Mostert, W., & Deike, L. (2020). Inertial energy dissipation in shallow-water breaking waves. *Journal of Fluid Mechanics*, *890*, A12.

21. Losada, M. A., Vidal, C., & Medina, R. (1989). Experimental study of the evolution of a solitary wave at an abrupt junction. *Journal of Geophysical Research: Oceans*, *94*(C10), 14557-14566.

22. Goring, D. G., & Raichlen, F. (1992). Propagation of long waves onto shelf. *Journal of waterway, port, coastal, and ocean engineering*, *118*(1), 43-61.

23. Giniyatullin, A. R., Kurkin, A. A., Semin, S. V., & Stepanyants, Y. A. (2014). Transformation of narrowband wavetrains of surface gravity waves passing over a bottom step. *Mathematical Modelling of Natural Phenomena*, *9*(5), 73-82.

24. Gorban, I. M. (2015). A numerical study of solitary wave interactions with a bottom step. *Continuous and Distributed Systems II: Theory and Applications*, 369-387.

25. Kurkin, A. A., Semin, S. V., & Stepanyants, Y. A. (2015). Transformation of surface waves over a bottom step. *Izvestiya, Atmospheric and Oceanic Physics*, *51*(2), 214-223.

26. Li, Y., Draycott, S., Zheng, Y., Lin, Z., Adcock, T. A., & Van Den Bremer, T. S. (2021). Why rogue waves occur atop abrupt depth transitions. *Journal of Fluid Mechanics*, *919*, R5.

27. Draycott, S., Li, Y., Stansby, P., Adcock, T., & van den Bremer, T. (2022, May). Harmonic-induced wave breaking due to abrupt depth transitions. In *EGU General Assembly Conference Abstracts* (pp. EGU22-9460).

28. Grilli, S. T., Losada, M. A., & Martin, F. (1993). Wave impact forces on mixed breakwaters. In *Coastal Engineering 1992* (pp. 1161-1174).

29. Liu, Y., & Li, Y. C. (2011). Wave interaction with a wave absorbing double curtain-wall breakwater. *Ocean Engineering*, *38*(10), 1237-1245.

30. Mohanlal, S., Harris, J. C., Yates, M. L., & Grilli, S. T. (2023). Unified depth-limited wave breaking detection and dissipation in fully nonlinear potential flow models. *Coastal Engineering*, *183*, 104316.

31. Song, C., & Sirviente, A. I. (2004). A numerical study of breaking waves. *Physics of fluids*, *16*(7), 2649-2667.

32. Emarat, N., Forehand, D. I., Christensen, E. D., & Greated, C. A. (2012). Experimental and numerical investigation of the internal kinematics of a surf-zone plunging breaker. *European Journal of Mechanics-B/Fluids*, *32*, 1-16.

33. Deike, L., Popinet, S., & Melville, W. K. (2015). Capillary effects on wave breaking. *Journal of Fluid Mechanics*, *769*, 541-569.

34. Deike, L., Melville, W. K., & Popinet, S. (2016). Air entrainment and bubble statistics in breaking waves. *Journal of Fluid Mechanics*, *801*, 91-129.

35. Mostert, W., Popinet, S., & Deike, L. (2022). High-resolution direct simulation of deep water breaking waves: transition to turbulence, bubbles and droplets production. *Journal of Fluid Mechanics*, *942*, A27.

36. Iafrati, A. (2009). Numerical study of the effects of the breaking intensity on wave breaking flows. *Journal of Fluid Mechanics*, *622*, 371-411.

37. Peregrine, D. H. (1998). Surf zone currents. *Theoretical and computational fluid dynamics*, *10*(1), 295-309.

38. Brocchini, M. (2013). A reasoned overview on Boussinesq-type models: the interplay between physics, mathematics and numerics. *Proceedings of the Royal Society A: Mathematical, Physical and Engineering Sciences*, *469*(2160), 20130496.

39. Duncan, J. H. (1981). An experimental investigation of breaking waves produced by a towed hydrofoil. *Proceedings of the Royal Society of London. A. Mathematical and Physical Sciences*, *377*(1770), 331-348.

40. Duncan, J. H. (1983). A note on the evaluation of the wave resistance of two-dimensional bodies from measurements of the downstream wave profile. *Journal of Ship Research*, *27*(02), 90-92.

41. Kennedy, A. B., Chen, Q., Kirby, J. T., & Dalrymple, R. A. (2000). Boussinesq modeling of wave transformation, breaking, and runup. I: 1D. *Journal of waterway, port, coastal, and ocean engineering*, *126*(1), 39-47.

42. Phillips, O. M. (1985). Spectral and statistical properties of the equilibrium range in wind-generated gravity waves. *Journal of Fluid Mechanics*, *156*, 505-531.

43. Whitham, G. B. (2011). *Linear and nonlinear waves*. John Wiley & Sons.

44. Tissier, M., Bonneton, P., Marche, F., Chazel, F., & Lannes, D. (2012). A new approach to handle wave breaking in fully non-linear Boussinesq models. *Coastal Engineering*, *67*, 54-66.

45. Booij, N. R. R. C., Ris, R. C., & Holthuijsen, L. H. (1999). A third-generation wave model for coastal regions: 1. Model description and validation. *Journal of geophysical research: Oceans*, *104*(C4), 7649-7666.

46. Drazen, D. A., Melville, W. K., & Lenain, L. U. C. (2008). Inertial scaling of dissipation in unsteady breaking waves. *Journal of fluid mechanics*, *611*, 307-332.

47. Romero, L., Melville, W. K., & Kleiss, J. M. (2012). Spectral energy dissipation due to surface wave breaking. *Journal of Physical Oceanography*, *42*(9), 1421-1444.

48. Romero, L. (2019). Distribution of surface wave breaking fronts. *Geophysical Research Letters*, *46*(17-18), 10463-10474.

49. Martins, K., Blenkinsopp, C. E., Deigaard, R., & Power, H. E. (2018). Energy dissipation in the inner surf zone: New insights from Li DAR-based roller geometry measurements. *Journal of Geophysical Research: Oceans*, *123*(5), 3386-3407.

50. Pizzo, N., & Melville, W. K. (2019). Focusing deep-water surface gravity wave packets: wave breaking criterion in a simplified model. *Journal of Fluid Mechanics*, *873*, 238-259.

51. Sinnis, J. T., Grare, L., Lenain, L., & Pizzo, N. (2021). Laboratory studies of the role of bandwidth in surface transport and energy dissipation of deep-water breaking waves. *Journal of Fluid Mechanics*, *927*, A5.

52. Barthelemy, X., Banner, M. L., Peirson, W. L., Fedele, F., Allis, M., & Dias, F. (2018). On a unified breaking onset threshold for gravity waves in deep and intermediate depth water. *Journal of Fluid Mechanics*, *841*, 463-488.

53. Popinet, S. (2003). Gerris: a tree-based adaptive solver for the incompressible Euler equations in complex geometries. *Journal of computational physics*, *190*(2), 572-600.

54. Bell, J. B., Colella, P., & Glaz, H. M. (1989). A second-order projection method for the incompressible Navier-Stokes equations. *Journal of computational physics*, *85*(2), 257-283.

55. Popinet, S. (2009). An accurate adaptive solver for surface-tension-driven interfacial flows. *Journal of Computational Physics*, *228*(16), 5838-5866.

56. Brackbill, J. U., Kothe, D. B., & Zemach, C. (1992). A continuum method for modeling surface tension. *Journal of computational physics*, *100*(2), 335-354.

57. Van Hooft, J. A., Popinet, S., Van Heerwaarden, C. C., Van der Linden, S. J., De Roode, S. R., & Van de Wiel, B. J. (2018). Towards adaptive grids for atmospheric boundary-layer simulations. *Boundary-layer meteorology*, *167*, 421-443.

58. Le Métayer, O., Gavrilyuk, S., & Hank, S. (2010). A numerical scheme for the Green–Naghdi model. *Journal of Computational Physics*, *229*(6), 2034-2045.

59. Pizzo, N. E., & Melville, W. K. (2013). Vortex generation by deep-water breaking waves. *Journal of fluid mechanics*, *734*, 198-218.

60. New, A. L., McIver, P., & Peregrine, D. H. (1985). Computations of overturning waves. *Journal of Fluid Mechanics*, *150*, 233-251.

61. Duncan, J. H., Philomin, V., Behres, M., & Kimmel, J. (1994). The formation of spilling breaking water waves. *Physics of fluids*, *6*(8), 2558-2560.

62. Hu, Z. Z., Mai, T., Greaves, D., & Raby, A. (2017). Investigations of offshore breaking wave impacts on a large offshore structure. *Journal of Fluids and Structures*, *75*, 99-116.

63. Beji, S. (1995). Note on a nonlinearity parameter of surface waves. *Coastal engineering*, *25*(1-2), 81-85.

64. Banner, M. L., & Peirson, W. L. (2007). Wave breaking onset and strength for two-dimensional deep-water wave groups. *Journal of Fluid Mechanics*, *585*, 93-115.

65. Grare, L., Peirson, W. L., Branger, H., Walker, J. W., Giovanangeli, J. P., & Makin, V. (2013). Growth and dissipation of wind-forced, deep-water waves. *Journal of Fluid Mechanics*, *722*, 5-50.

66. Derakhti, M., & Kirby, J. T. (2016). Breaking-onset, energy and momentum flux in unsteady focused wave packets. *Journal of Fluid Mechanics*, *790*, 553-581.

67. Derakhti, M., Kirby, J. T., Banner, M. L., Grilli, S. T., & Thomson, J. (2020). A unified breaking onset criterion for surface gravity water waves in arbitrary depth. *Journal of Geophysical Research: Oceans*, *125*(7), e2019JC015886.

68. Pizzo, N., Murray, E., Smith, D. L., & Lenain, L. (2021). The role of bandwidth in setting the breaking slope threshold of deep-water focusing wave packets. *Physics of Fluids*, *33*(11).

69. Robertson, B., Hall, K., Zytner, R., & Nistor, I. (2013). Breaking waves: Review of characteristic relationships. *Coastal Engineering Journal*, *55*(01), 1350002.

Acknowledgments

Numerical simulations in this project were performed using the Foundry cluster at Missouri University of Science and Technology, which is supported by the National Science Foundation under Grant No. OAC-1919789. The authors appreciate the financial support from the Mid-American Transportation Center, through the MATC project starting in 2021, “Understanding of Bridge Vulnerability to Climate Change Enables Pro-active Adaptation Measures”.

Appendix A Convergence Study

The meshes used for these simulations are square, such that $\Delta x = \Delta y$. Our choice of mesh size is related to the numerical convergence. We followed the process used in Mostert and Deike [20] to measure the numerical convergence based on the energy budget. The kinetic and gravitational potential energies, E_k and E_p, are

$$E_k = \frac{1}{2}\int_V \rho|\boldsymbol{u}\cdot\boldsymbol{u}|\,dV, \quad E_p = \int_V \rho g y\,dV - E_{p0}, \quad E = E_k + E_p. \tag{A.1}$$

In Figure 4.8, we show a comparison of energy budget convergence for two cases: one with a 2° beach slope and 0.2 initial wave amplitude, and one with 4° beach slope and 0.4 initial wave amplitude. Both cases have a storm surge depth of 0.3. In both cases, we compare mesh sizes of $\Delta x = L_0/2^{13}$ and $\Delta x = L_0/2^{14}$, where L_0 is the length of the domain. We see that there is little difference between the energy dissipation between the two resolutions and thus conclude that these simulations converge for a resolution of 2^{13}.

Appendix B Additional Breaker Interface Plots

Figure B.1 shows a case with a negative storm surge depth. Here the beach slope is θ = 2º, the initial wave amplitude is a_0/h_0 = 0.5, and the storm surge depth is h_s/h_0 =−0.1, i.e., the inshore region lies above the undisturbed water level. In this case the wave breaks on the beach slope. The air cavities observed in Figure B.1(d) indicate this is a plunging breaker. This behavior is similar to the cases presented in Mostert and Deike [20], in which the bathymetry does not include an inshore region, so that the wave breaks directly on the beach slope.

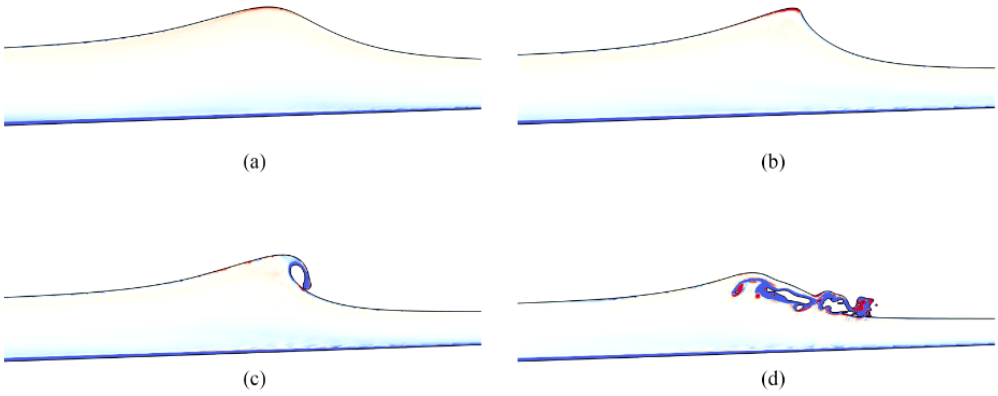

Figure B.1 Wave breaking process (plunging breaker) for the case with a beach slope of 2°, an initial wave amplitude of 0.5, and a storm surge depth of −0.1. Vorticity (color contour) in the water phase at the following four time instants: (a) t/t_0 = 13.2, (b) t/t_0 = 15.6, (c) t/t_0 = 17.2, and (d) t /t0 = 19.0.